Modulation of Surface Gravity Waves by Internal Waves

LUC LENAIN[a] AND NICK PIZZO[a]

[a] *Scripps Institution of Oceanography, La Jolla, California*

ABSTRACT: Internal waves are a regular feature of the open-ocean and coastal waters. As a train of internal waves propagates, their surface induced currents modulate the surface waves, generating a characteristic rough- and smooth-banded structure. While the surface expression of these internal waves is well known and has been observed from a variety of remote sensing instruments, direct quantitative observations of the directional properties of the surface gravity wave field modulated by an internal wave remain sparse. In this work, we report on a comprehensive field campaign conducted off the coast of Point Sal, California, in September 2017. Using a unique combination of airborne remote sensing observations, along with in situ surface and subsurface measurements, we investigate and quantify the interaction between surface gravity and internal wave processes. We find that surface waves are significantly modulated by the currents induced by the internal waves. Through novel observations of ocean topography, we characterize the rapid modification of the directional and spectral properties of surface waves over very short spatial scales [$O(100)$ m or less]. Over a range of wavelengths (3–9-m waves), geometrical optics and wave action conservation predictions show good agreement with the observed wavenumber spectra in smooth and rough regions of the modulated surface waves. If a parameterization of wave action source terms is used, good agreement is found over a larger range of wavenumbers, down to 4 rad m^{-1}. These results elucidate properties of surface waves interacting with a submesoscale ocean current and should provide insight into more general interactions between surface waves and the fine-scale structure of the upper ocean.

KEYWORDS: Currents; Internal waves; Waves, oceanic; Air–sea interaction; Remote sensing

1. Introduction

The inner shelf is bounded on the shoreward side by the surf zone and offshore by a depth of approximately 50–100 m. This is a region in which a rich collection of physical processes can occur over a broad range of time scales (from fractions of a second for wave breaking to the two-week spring–neap tidal cycle and seasonal cycles), and length scales (millimeters for the wind stress supporting gravity-capillary waves and other microstructure to $O(10–100)$ km for along-and across-shelf processes) associated with a wide variety of different forcing mechanisms. The ability to observe these processes with moored water-column measurements or research vessels is limited due to access and/or cost. This then places more emphasis on remote sensing techniques and the use of autonomous platforms. However, given the fast time scales of many of these oceanographic processes relative to the time scales of repeat satellite coverage, the role of standard satellite remote sensing is limited, thus highlighting the importance of airborne remote sensing, either by crewed or uncrewed aircraft.

Many of the current ocean remote sensing techniques are indirect and are dependent on modeling or empirical correlations of surface "roughness" with backscatter cross section or are based on assumptions about the speed of the scatterers relative to the underlying current and the surface wind drift. Since this indirect remote sensing depends to a significant

extent on the surface wave and temperature fields, as well as their modulation by other physical processes, research into ocean surface signatures requires in situ measurements of the lower marine atmospheric boundary layer and the surface waters before the full fidelity of these techniques can be established.

Unlike the scattering methods discussed above, airborne lidar directly measures the short surface waves. This includes the modulation of the surface gravity waves by internal waves (hereinafter denoted IW) as well as the IW-induced ocean-surface displacement (setup and setdown) that may be $O(1)$ cm or more on the continental shelf (Helfrich and Melville 2006; Melville et al. 2016). There is a striking similarity between surface waves modulated by IW and surface waves modulated at submesoscale fronts (Romero et al. 2017). These surface wave–IW interactions [where here the IW can have variations that are $O(100)$ m or less] act as a simple case of waves interacting with a more general submesoscale feature, because the IW are often quasi two-dimensional and have their own dynamics that are relatively well understood as compared with the dynamics of submesoscale jets, filaments, and fronts (McWilliams 2016).

Early theories examining wave–current interactions were based on geometrical optics and wave action conservation (Longuet-Higgins and Stewart 1962, 1964; Bretherton and Garrett 1968; Phillips 1966). With the advent and increased use of radars [e.g., synthetic aperture radar (SAR) and ship-based X band] the characteristic smooth and rough bands present in surface waves due to IW-induced currents has been well documented (e.g., Osborne and Burch 1980; Alpers 1985; Thompson and Gasparovic 1986; Plant et al. 2010). The theory developed to explain these observations is also based on

---

FIG. 1. A handheld photograph taken from the research aircraft at 2348 UTC 13 Sep 2017, flying at an elevation of ~1500 ft above the internal wave packet considered in this analysis. The roughening and smoothing of the surface into well-defined bands is distinct. Also note the convergence of surfactants (e.g., foam and biological matter) forming sharp white lines, and the lateral extent of the wave packet. Swell is coming from the northwest, while shorter wind waves are aligned with the direction of propagation of the IW, coming from the west.

geometrical optics and wave action conservation, but additionally it is often assumed that the current-modulated spectrum deviates only a small amount from the unmodulated spectrum (Phillips 1984; Alpers 1985) and this is known as the relaxation approximation. These theories suffer from several short comings that vary in severity depending on the situation under consideration. First, these phase averaged theories do not account for bound and reflected surface waves (McKee 1975; Smith 1983). Second, the assumption that the modulated spectrum only deviates a small amount from the unmodulated spectrum may not hold for particularly strong interactions (e.g., it does not hold for the observations presented here). Third, there is currently no axiomatic way to model the source terms (wind input, wave–wave interactions, and wave dissipation). This may be particularly troublesome here, as surface wave breaking often characterizes the rough bands that arise in these modulations.

Some of these shortcomings were addressed in the phase-resolved model of Craig et al. (2012), who modeled the resonant interaction of nonlinear internal waves with the surface waves, where the surface signature is generated by a process analogous to radiative absorption. Note, Craig et al. (2012) assumed that both the surface and internal wave field were at most weakly nonlinear and assumed that the surface wave field was narrow-banded. More recently, Hao and Shen (2020) performed direct numerical simulations of a two-layer model to investigate the surface roughness signature induced by an internal wave. Their model did not include steep and breaking waves. Both of these studies found that the banded structure (i.e., smooth and rough bands) observed in the surface wave field can be generated by a conservative mechanism. Note, the model of Craig et al. (2012) requires detailed in situ measurements of the upper water column, while the numerical model of Hao and Shen (2020) is computationally expensive. Furthermore, recently Jiang et al. (2019) investigated the generation of (weakly nonlinear) surface waves at the leading edge of an internal wave. These models do not apply to the physical scenario considered here, where we have a broad band sea state that is characterized by breaking in the rough bands (see Fig. 1).

In the current study, we characterize and investigate the directional properties of a surface gravity wave field modulated by an IW during an experiment conducted off the coast of Point Sal, California, in the autumn of 2017 using a combination of airborne remote sensing techniques along with in situ surface and subsurface measurements. Classical geometrical optics and wave action conservation are tested for this data and agreement over a limited range of wavenumbers is found. To model the higher wavenumbers an empirical viscosity is employed, and this method is found to give good agreement with the data over a larger range of wavenumbers.
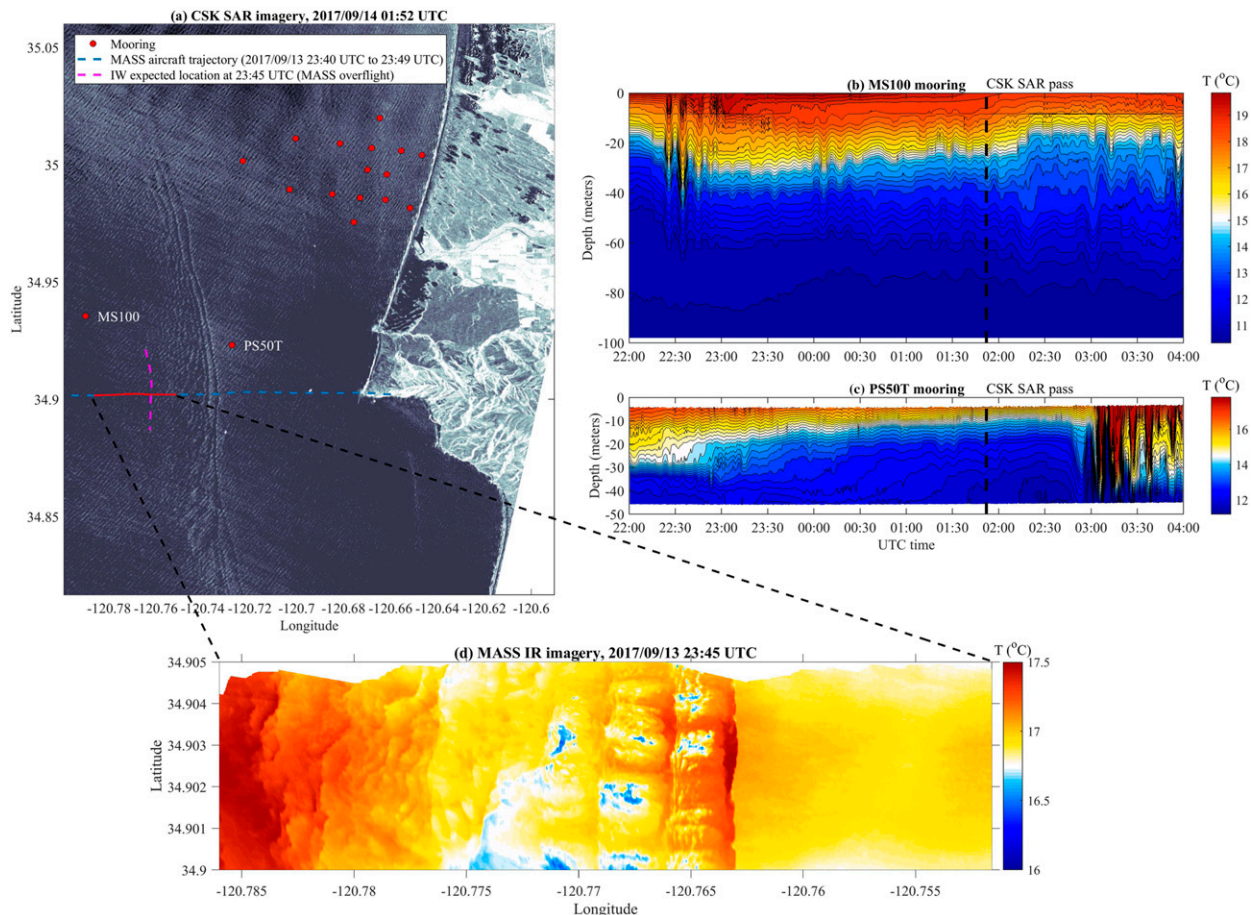
FIG. 2. (a) A CSK SAR image recorded at 0152 UTC 14 Sep 2017 showing a packet of high-frequency internal waves propagating toward Point Sal during the Innershelf DRI experiment. Also shown are the locations of a selected number of moorings deployed during the field programs (red dots). The temperature profiles collected at two of those sites, (b) MS100 and (c) PS50T, respectively located at 100- and 50-m water depth, capturing the evolution of the internal waves as they propagate toward shore, with the time of the SAR imagery overpass indicated by the dashed line. (d) Infrared imagery of the same packet of internal waves at 2345 UTC 13 Sep 2017, approximately 2 h before the SAR image depicted in (a). The location of the flight track and the expected location of the front of the internal wave based on the propagation speed computed from the mooring are also shown in (a).

The experiment, instrumentation, environmental conditions, and processing techniques are presented in section 2. Section 3 describes the observed directional properties of surface gravity waves under the influence of an internal wave packet. Geometrical optics and wave action predictions are presented in section 4, and the findings are further discussed and summarized in section 5.

2. Methods

a. Experiment

The present study is based on data collected during the ONR-funded Innershelf Directed Research Initiative (DRI) program (Kumar et al. 2021). The primary objective of this project was to investigate and observe (particularly from an airborne platform) the role of surface and internal wave processes on the dynamics, transport, currents and mixing in the

water column on the inner shelf. Airborne remote sensing measurements were collected from 5 to 21 September 2017 off the coast of Point Sal using the Modular Aerial Sensing System (MASS; Melville et al. 2016). The field program included a large number of deployed moorings and drifters, an array of land-based radars, and intensive ship-based upper-ocean measurements. Atmospheric surface conditions were estimated from the MASS (Lenain et al. 2019b).

b. Instrumentation

The MASS (Melville et al. 2016), a compact airborne remote sensing instrument package, was installed on board a Partenava P68 aircraft for the flights in September 2017. At the heart of the MASS instrument package is Riegl's LMS-Q680i, a long-range airborne laser scanner (lidar) with 1550-nm wavelength for retrieving ocean surface or land topography. The scanner has a maximum pulse repetition rate of 400 kHz over a ±30°
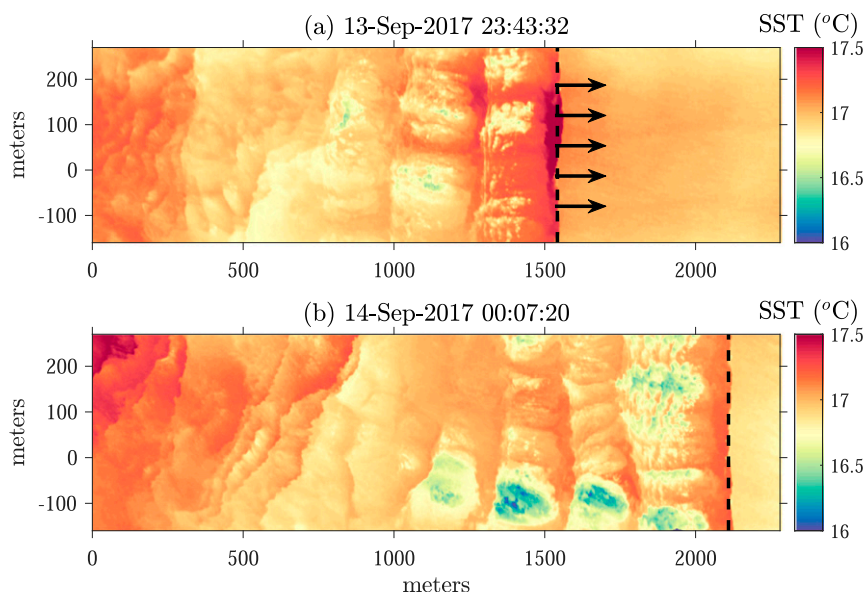
FIG. 3. Sea surface temperature image of the internal wave packet shown in Figs. 1 and 2, collected from the MASS IR camera at two different times, approximately 24 min apart. Horizontal axis x and vertical axis y are aligned with the east (positive) and north (positive), and the origin of the reference frame was chosen arbitrarily, approximately 11 km straight west of Point Sal. The wave is propagating at a speed $C = 0.4 \, \mathrm{m \, s^{-1}}$ toward the east. Note the pronounced transverse structures, especially in (b).

cross-flight direction field of view that is scanned at up to 200 lines per second, producing a swath width that is roughly equivalent to the plane's altitude.

A forward-looking infrared (FLIR) SC6000 longwave infrared camera with a quantum well infrared photodetector (14-bit, 640×512 pixel resolution output at up to 125 Hz) was used to produce images of sea surface temperature (SST). During this experiment, SST maps were produced from georeferenced infrared images collected at 50 Hz and then conditionally averaged to improve the signal-to-noise ratio. Assuming an aircraft speed of $50 \, \mathrm{m \, s^{-1}}$, this leads to a range of approximately 500–2000 frames contributing to each pixel of the SST map, depending on the flight altitude.

A Specim AisaKESTREL hyperspectral camera that operates in the 400–1000-nm spectral range with 0.88-nm native spectral resolution and 2048-pixel native swath resolution was also used during the experiment. The 12-bit push-broom imager operates at up to 100 Hz (typically 80 Hz) with a 35-mm lens that yields a 40° cross-track field of view. Coupled with the camera system is a fiber-optic downwelling irradiance sensor (FODIS) that was installed on top of the fuselage of the aircraft with 1-Hz acquisition that was synchronized to the hyperspectral camera, allowing for absolute radiance estimates from the combination of the radiometrically corrected hyperspectral imagery and incoming radiance data. Chlorophyll-a (Chl-a) concentration is derived using the OCx band algorithm (https://oceancolor.gsfc.nasa.gov/atbd/chlor_a/), used to compute Chl-a concentration from the MODIS *Aqua* satellite.

The MASS instrument is also equipped with an IO Industries Flare 12M125 4096×3072 pixel resolution, 10-bit monochrome

video camera that operates at up to 100 Hz (typically 5 Hz) with a CMOS sensor that has a 5.5-μm pixel size. The camera body has a built-in Birger Engineering EF-mount lens adapter for electronic control of its Canon EF 14-mm f/2.8L II USM lens that has a 78° cross-track by 62° along-track field of view. A custom mount for an electronically controlled circular polarizing filter was also installed just offset from the lens to minimize sun glare.

A Novatel LN200 tactical-grade inertial measurement unit (IMU) is a crucial component of the MASS instrument. This IMU contains closed-loop fiber optic gyros and solid-state silicon accelerometers with 200-Hz data output rates. The IMU is coupled with a Novatel PwrPak7 dual-antenna GPS receiver, with Novatel's SPAN firmware enabled to merge IMU and GPS data streams, leveraging the advantages of each technology and offering a fused postprocessed trajectory solution that is both reliable and highly accurate (Melville et al. 2016; Lenain and Melville 2017; Lenain and Pizzo 2020).

3. Observations

In this study, we focus on an IW packet that was propagating toward Point Sal on 13 and 14 September 2017, observed from the MASS during two collocated overflights conducted approximately 25 min apart at 2343 UTC 13 September and 0007 UTC 14 September. The IW is clearly visible in Fig. 1, which shows a photograph from a handheld camera taken from the research aircraft flying at 1500 ft (~460 m) MSL, with the camera pointing approximately toward the north. We find the characteristic surface roughness signature of IWs, that is, a

series of rough and smooth bands with areas of intense convergence between them, highlighted by lines of dense surface foam and concentrated biological matter. Also, we qualitatively note the directionality of the surface wave field, with short wind-waves aligned with the IW propagating to the east while the swell comes from the northwest. Rough bands of the wave field exhibit intense small-scale breaking while the shorter wind-waves appear completely suppressed in the smooth bands. Last, we note the significant lateral extent of the IW. For reference, surface winds measured by the MASS instrument (Lenain et al. 2019b) at the time of the overflights were in the range of 5–6 m s^{-1}.

a. Remote sensing and mooring observations

The IW packet was captured in CSK SAR imagery (CSTARS, University of Miami) approximately 2 h after the aircraft overflights, at 0152 UTC 14 September 2017. This is shown in Fig. 2a, along with the aircraft track (blue dashed line) and the location of two moorings equipped with thermistor chains deployed at 50- and 100-m water depth, labeled PS50T and MS100, respectively. Temperature profiles at these two locations are shown in Figs. 2b and 2c, which display the rapid evolution of the IW packet as it travels from the 100-m isobath to the 50-m isobath, toward Point Sal. Sea surface temperature (SST) information collected from the MASS is presented in Fig. 2d, corresponding to the portion of flight track highlighted in red in Fig. 2a. Note, the airborne survey and the SAR overpass were not performed simultaneously, which explains why the internal wave packet appears at two different locations in these two products. For reference, the location of the flight track and the expected location of the front of the IW at the time of the flight, based on the propagation speed computed from the mooring observations, is also shown. This is in qualitative agreement with the location of the IW front found in the MASS SST image.

The propagation speed of the IW packet is estimated using collocated SST images from the two MASS overflights (Fig. 3) taken approximately 24 min apart, by tracking the position of the thermal surface signature of the IW packet over this temporal interval. We find a propagation speed C of approximately 0.4 m s^{-1}, toward the east, which is consistent with what can be inferred from the mooring observations. Also note the modulation of surface temperature structures by the IW packet. We find areas of cooler water brought to the surface from the mixing caused by the IW as it propagates toward shore, exhibiting transverse "horseshoe-like" structures, hinting at the complex mixing dynamics and flow circulation that is occurring, which is further discussed in section 5.

Figure 4 shows vertical profiles of temperature and currents in a coordinate system oriented in the direction of propagation of the IW at mooring MS100 (100-m depth) collected from 2000 UTC 13 September through 0130 UTC 14 September 2017. The IW packet crosses the mooring around 2230 UTC and extends from the surface down to the bottom, as is shown in the observations of along-wave current velocity (Fig. 4b). After its passage, we observe a restratification of the water column, with a shoreward surface current compensated by offshore flow at depth. McSweeney et al. (2020) used an array
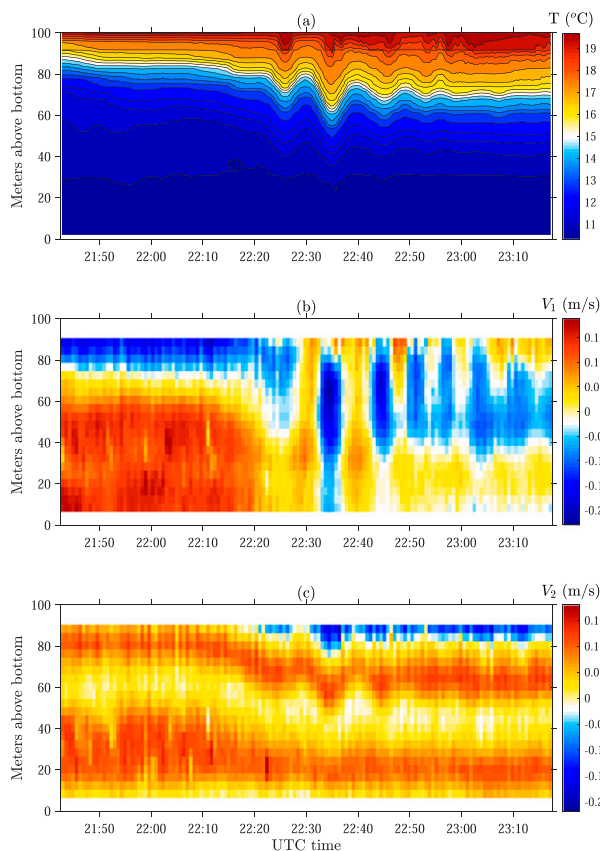

FIG. 4. Vertical profiles of (a) temperature and currents in a coordinate system of the direction of propagation of the internal wave, (b) V_1 along and (c) V_2 cross, collected from the MS100 mooring on 13–14 Sep 2017, located at approximately 100-m depth as shown in Fig. 2a. Note the passage of the very energetic internal wave packet, considered here, around 2230–2300 extending from the surface down to the bottom (i.e., see along-wave direction current profiles).

of 15 moorings (including the MS100 one considered here) deployed as part the Innershelf DRI program to characterize the cross-shore structure and evolution of large-amplitude internal waves as they transit across the inner shelf.

b. Surface signature of the internal wave packet

In this section we focus on the surface expression of the IW packet captured at 2340 UTC 13 September 2017 (first overflight). Sea surface temperature, visible (RGB) imagery, Chl-a concentration, and wave steepness computed from the lidar-derived surface topography are presented in Figs. 5a–d, respectively. The wave steepness S is defined here as

$$S = \sqrt{\left(\frac{\partial \eta}{\partial x}\right)^2 + \left(\frac{\partial \eta}{\partial y}\right)^2}, \qquad (1)$$

where $\eta = \eta(x, y)$ is the surface displacement measured from the airborne lidar. Here $dx = dy$ and is set to 0.2 m, the highest spatial resolution achievable by the instrument flying at 1500 ft
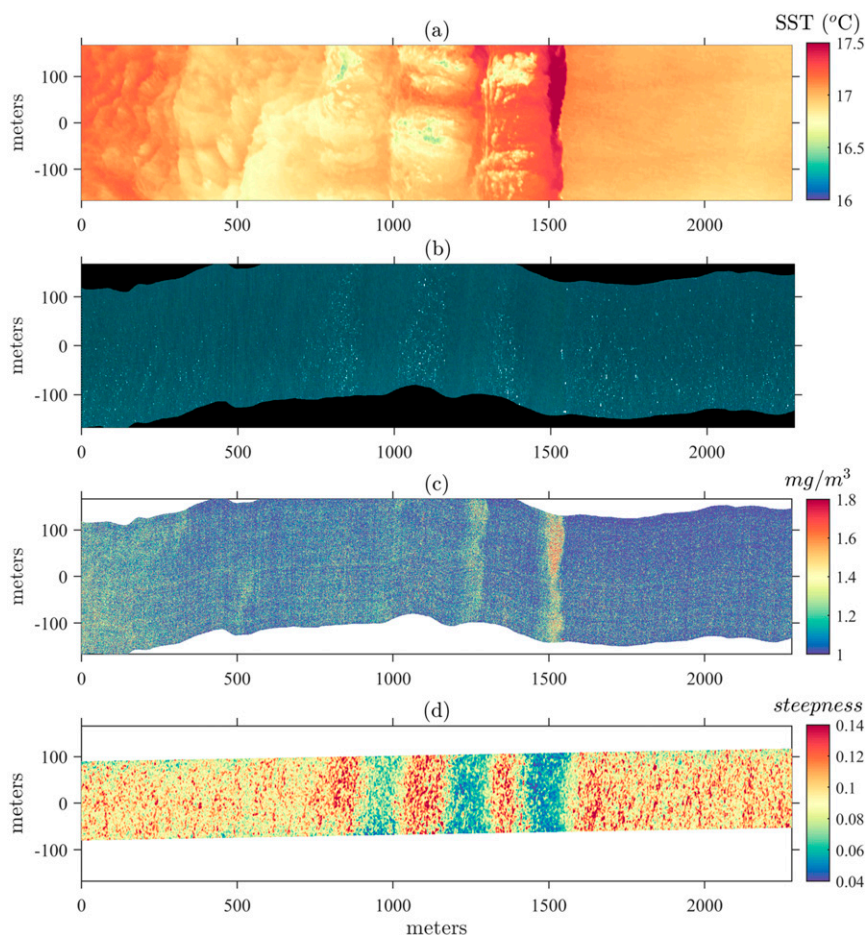
FIG. 5. Surface signatures of the internal wave packet at 2340 UTC 13 Sep 2017. (a) Sea surface temperature, (b) visible (RGB) imagery, (c) Chl-*a* concentration, and (d) wave steepness S computed from the lidar-derived surface topography. Note the presence of rough and smooth bands in (b), also showing an increased amount of whitecap coverage. Next, we find increased concentration of Chl-*a* in the smooth bands, as shown in (c). Last, the modulation of the surface gravity waves from the internal waves is clear in (d), where we find suppression of the high-frequency waves in the smooth bands and increased steepness in the rough bands.

MSL. The rough and smooth bands, classical surface expressions of an IW packet, are clearly identified in all imagery products. Visible imagery (Fig. 5b) shows an increase in whitecapping in the rough bands, while no whitecapping is observed in the smooth bands. We find patches of concentrated surface Chl-*a* in the smooth bands, as it gets collected in convergence zones (Fig. 5c). These elevated values also coincide with an apparent increase in sea surface temperature (Fig. 5a). Two possible explanations are either a more efficient surface heating from the smooth ocean surface as compared with the rough bands, combined with increased heat absorption from the surface Chl-*a* concentrated areas, or a measurement artifact associated with the observation technique (infrared camera), as any change in the emissivity across the infrared images is not accounted for. In the last panel, the steepness S exhibits alternating bands of steep and

gently sloped waves, with a magnitude rapidly attenuated by more than 50% in the smooth bands, and an amplified by 10%–20% in the rough bands.

c. Modulation of surface gravity waves

1) MEAN-SQUARE SLOPE

Here, the properties of surface slope are examined using lidar surface topography. With this approach, the contribution of surface waves shorter than $dx/2 = dy/2 = 0.1$ m, the highest spatial resolution achievable with the lidar for the considered flight altitude, is not included and we therefore expect for the mean-square slope to be underestimated by 10%–20% for the conditions experienced when the measurements were collected (Lenain and Melville 2017). Note that the mean-square slope calculation method described in Lenain et al. (2019b) could

not be applied to this dataset because the surface slope was evolving too rapidly in space to obtain meaningful slope distributions. The mean-square slope in the upwind and crosswind directions is defined as

$$\sigma_u^2 = \left\langle \left(\frac{\partial \eta}{\partial x}\right)^2 \right\rangle \quad \text{and} \quad \sigma_c^2 = \left\langle \left(\frac{\partial \eta}{\partial y}\right)^2 \right\rangle. \quad (2)$$

At the time of the IW overflight, the wind direction was pointing to the east, aligned with the x direction, while positive y is pointing toward the north. Wind measurements were obtained from NDBC station 46011, located 20 km upwind of the observation site, and showed a wind direction of 274° (coming from *true north*) at the time of the flight. Mean square slopes σ_c^2 and σ_u^2 across the IW packet for both crosswind and along-wind directions are shown in Fig. 6a. Note the rapid decrease of their magnitude in the smooth bands (almost 50% decrease over a few hundred meters), for both components, and larger slopes in the rough bands (see Fig. 5 for exact location of these bands with respect to the other imaging products), exhibiting up to a factor 2 increase over just a few hundreds of meters. These results show rapid modulation of surface roughness by IW-induced surface currents and demonstrate the general importance of the interaction of wave and currents (in particular, submesoscale currents) in modulating surface roughness.

The ratio $\gamma = \sigma_c^2/\sigma_u^2$, a measure of the directionality of the total surface slope [see, e.g., Cox and Munk (1954), Munk (2009), and Lenain et al. (2019b) for more discussions on this], is shown in Fig. 6b. Away from the influence of the IW packet, we find the value of this ratio to be approximately 0.6; this is lower than prior studies (Bréon and Henriot 2006; Cox and Munk 1954; Lenain et al. 2019b) but is not completely unexpected because the contribution from very short waves, that is, of less than 0.1-m wavelength, are not considered here. However, what is remarkable is the rapid evolution of γ resulting from the modulation by the currents induced by the IW packet. In smooth bands this ratio increases, reaching a value close to 1 because the directional distribution of the short surface waves is becoming nearly isotropic, whereas γ is smaller in the rough bands, implying that the directional spreading of the waves contributing to the slope is reduced and is mostly aligned with the wind, even in the saturation range where a bimodal distribution and significant directional spread are normally expected (Longuet-Higgins and Stewart 1962; Lenain and Melville 2017).

2) SURFACE WAVE SPECTRUM

Omnidirectional spectra of surface waves collected from the airborne lidar as a function of along-track distance are presented in Fig. 7d. Two-dimensional fast Fourier transforms were computed over 50 m × 50 m square areas of surface topography with 50% overlap to capture the rapidly evolving spectral properties of surface waves. All sections were first detrended, then tapered with a two-dimensional Hanning window, and finally padded with zeros (25%).

The omnidirectional wave spectrum $\phi(k)$ is defined as the azimuthally integrated directional spectrum,
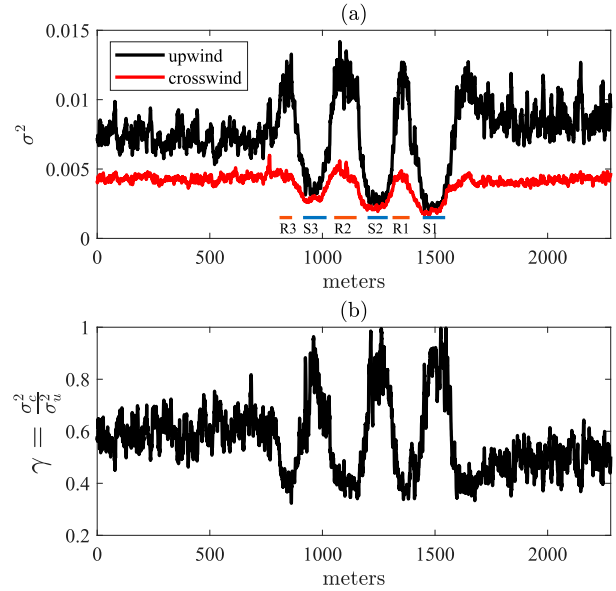

FIG. 6. Mean square slope σ_c^2 and σ_u^2 across the internal wave packet, computed for both crosswind and along-wind directions. (b) The ratio $\gamma = \sigma_c^2/\sigma_u^2$, a measure of the directionality of the total surface slope. The area used for the computation of the wave directional spectra in each smooth (S1, S2, and S3) and rough (R1, R2, and R3) band discussed in section 4 is also shown.

$$\phi(k) = \int_0^{2\pi} F(k,\theta)k\,d\theta, \quad (3)$$

where $F(k, \theta)$ is the wave directional spectrum. Omnidirectional wave spectra as a function of along-flight distance are shown in Fig. 7d. Cross-track averages of SST, Chl-a concentration, and steepness are also shown, along with whitecap coverage (%) computed from the visible imagery, following the method of Kleiss and Melville (2011), clearly showing the modulation of the surface conditions by the IW.

Surface velocities (positive, toward the east) in Fig. 7c are computed from the raw infrared images using correlation techniques, specifically based on an adaptive particle image velocimetry (PIV) algorithm similar to that described by Thomas et al. (2005), tracking temperature structures at the surface of the ocean instead of seeded particle patterns. Pairs of images separated by a set time $\Delta t = 5$ s are used, corresponding to the maximum achievable time difference under the flight conditions (constrained by the aircraft speed and altitude) to ensure sufficient overlap between individual images. We obtain a velocity field with a 2-m spatial resolution, subsequently averaged in the cross-track direction, while only retaining velocity estimates with PIV correlation values larger than 85%. The velocity field in areas with little or no temperature structures is much noisier or is not available, for example, for x larger than 1600 m in Fig. 7c. Additionally, since the spatial averaging is performed over a limited area, we expect nonnegligible contributions to these estimates from surface wave orbital motion and wave breaking–induced transport (Lenain and Melville 2017; Deike et al. 2017; Pizzo et al. 2019; Lenain et al. 2019a), that will produce a positive bias in surface velocities, toward
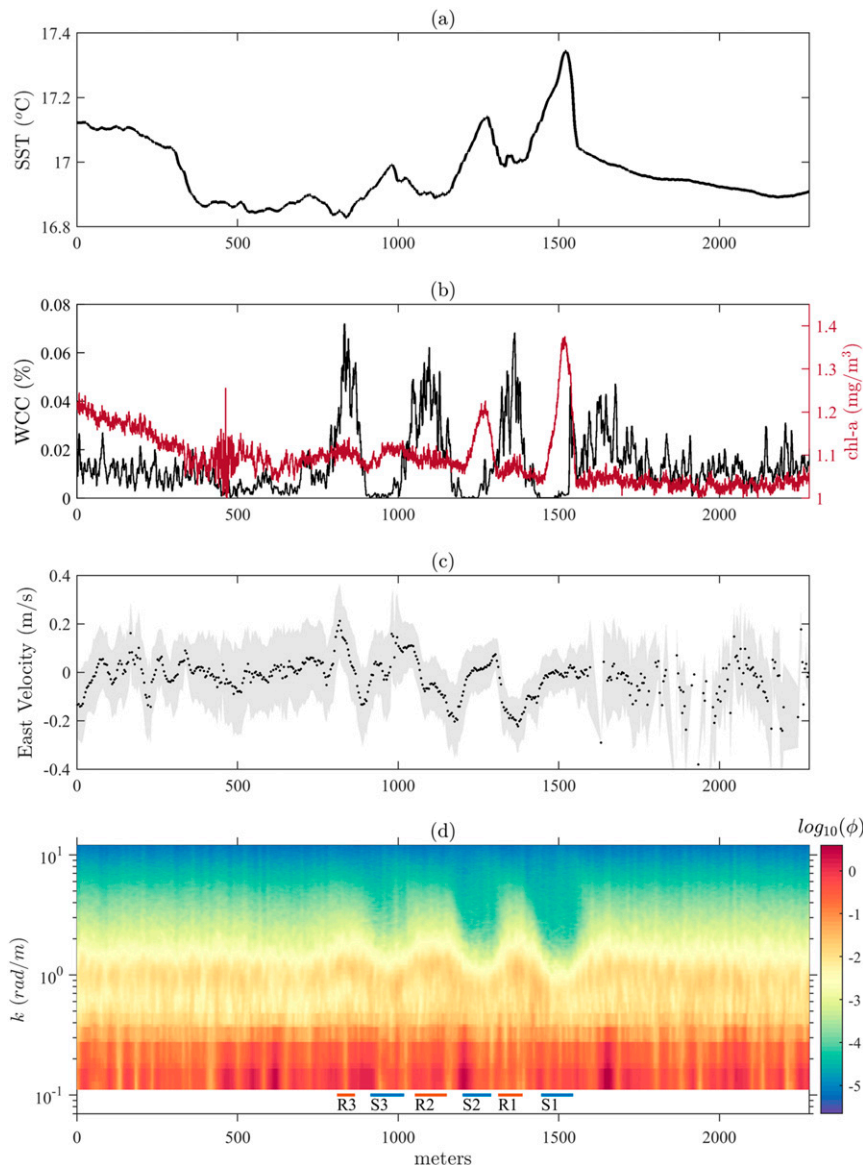
FIG. 7. (a) Cross-track average of the SST map presented in Fig. 5a. Note the clear modulation of the SST by the internal wave packet. (b) Whitecap coverage (WCC; %) and cross-track average Chl-*a* concentration, (c) surface velocity (east) computed from the IR images, and (d) the corresponding surface wave spectrogram along the flight track.

the east, the direction of propagation of wind-generated surface waves, especially in the rough bands, where wave breaking is present. Nevertheless, these estimates clearly show the modulation of surface velocities from the IW packet. The surface currents oppose the dominant direction of the waves in the rough bands, with speeds of up to approximately $-0.2\,\mathrm{m\,s^{-1}}$ in magnitude, and travel with the waves in the smooth bands, with a magnitude of up to about $0.2\,\mathrm{m\,s^{-1}}$. These estimates are generally consistent with the mooring observations presented in Fig. 4.

The spatial evolution of the omnidirectional wave spectrum $\phi(k)$ is presented in Fig. 7d, displaying a rapid modulation of

the high-frequency components—in particular, for wavenumbers in the 0.08–$8\,\mathrm{rad\,m^{-1}}$ range (approximately 6–0.6-m long waves). The wind-wave spectral peak, around $1\,\mathrm{rad\,m^{-1}}$, is rapidly changing, by as much as 30%, across the internal wave bands, and a severe reduction in spectral magnitude is found in the smooth bands for shorter waves ($>1\,\mathrm{rad\,m^{-1}}$). This is highlighted in Fig. 8, where omnidirectional spectra computed in smooth and rough bands are shown, along with a "background" spectrum, computed away from the influence of the internal waves, over a larger section of surface topography, to resolve longer wavelengths. Note that this background spectrum has a swell peak around 0.04–$0.05\,\mathrm{rad\,m^{-1}}$. Here, S_1, S_2,
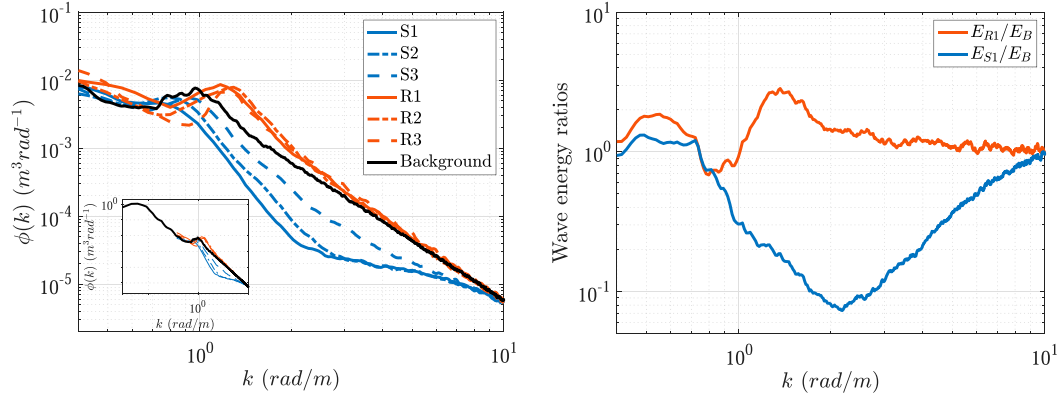
FIG. 8. (a) Omnidirectional spectra computed in rough and smooth bands. The background spectrum, computed in an area away from the influence of the internal wave packet, is shown in black. The numbered locations increase from east to west and correspond to the six bands shown in Fig. 7d. (b) The ratio of the energy density in the modulated bands to the energy density for the background sea state. We see that for the rough bands the ratio of these quantities may be $O(1)$.

and S_3 correspond to the smooth bands and increase in distance to the west with index (see Fig. 7d), and R_1, R_2, and R_3 correspond to the three rough bands. The rapid redistribution of the energy under the influence of the internal wave packet is remarkable. While the energy rapidly drops down for waves in the 0.08–8 rad m^{-1} range in the smooth bands, we find enhancement in the rough bands near the peak of the wind waves, along with a slight frequency shift. The ratio of the energy density of the rough and smooth bands, E_R and E_S, respectively, to the background action E_B, is shown in Fig. 8b. If we assume that the variations of the wave action, for k fixed,

are equivalent to those of the energy density (Alpers 1985), then this ratio shows that the deviations of energy, and hence action, in the rough bands are $O(1)$, implying that the surface wave field is not weakly modulated by the presence of the internal wave in this range of wavenumbers, as it is often assumed in relaxation theories (e.g., Alpers 1985; Rascle et al. 2016).

Directional wavenumber spectra $F(k_x, k_y)$ in rough and smooth bands are shown in Fig. 9, along with a spectrum computed away from the influence of the IW packet. Here k_x and k_y represent the positive east and north directions,
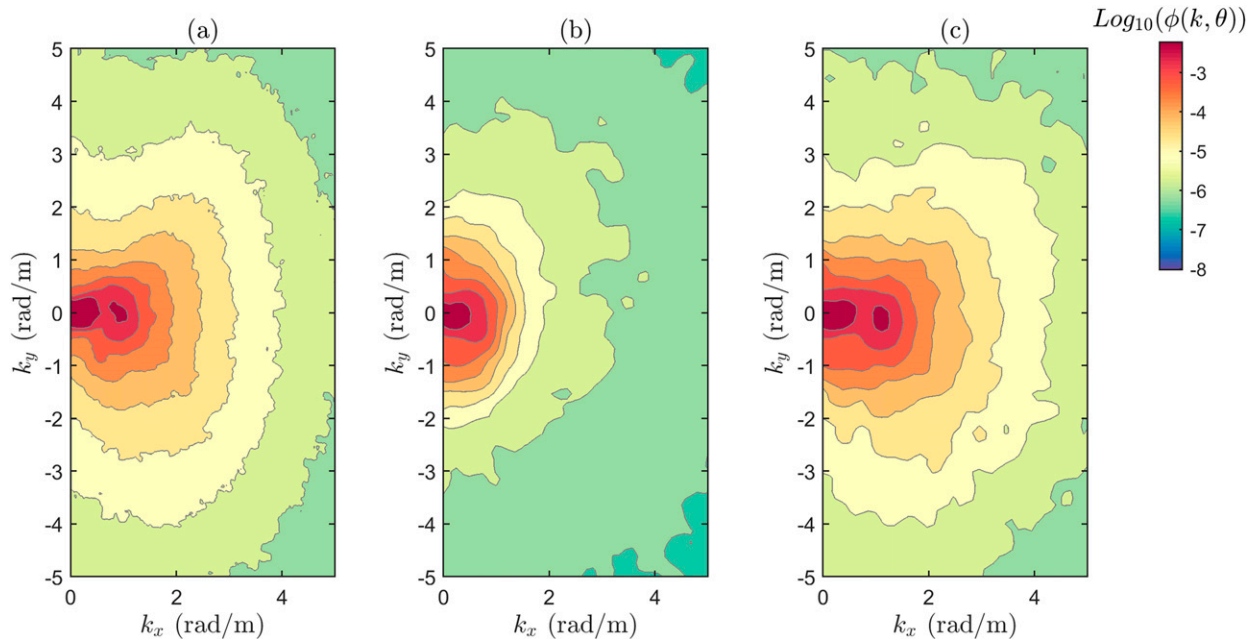

FIG. 9. Directional wavenumber spectrum $F(k_x, k_y)$, collected on 13 Sep 2017, of the surface wave field (a) away from the internal wave, (b) in a "smooth" band (S1), and (c) in a "rough" band (R1) of the internal wave packet.

respectively. For clarity of presentation, all three spectra are cropped at $5 \, \mathrm{rad \, m^{-1}}$.

Figure 9a shows two peaks corresponding to swell and wind-generated waves, along with a distinguishable bimodal distribution [see, e.g., Lenain and Melville (2017) for a detailed discussion on this topic]. The shape of the directional spectra computed in a rough band (Fig. 9c) exhibits a similar geometry, although with a frequency shift for the wind-generated wave peak, and a net decrease in angular separation between energy lobes as a function of wavenumber, particularly in the 2–$5 \, \mathrm{rad \, m^{-1}}$ range, as compared with the background spectrum plotted in Fig. 9a. On the other hand, the spectra computed in the smooth bands shows a rapid increase in angular lobe separation, in the 1–$2 \, \mathrm{rad \, m^{-1}}$ range, then a drop in spectral energy for larger wavenumbers. Note, the asymmetry in the k_y direction found at high frequencies is likely caused by short waves interacting with alongshore currents. Overall, these results suggest that, through wave–current interaction, the directional properties of the surface wave spectrum are rapidly modulated under the influence of the propagating IW packet. This is investigated further from a theoretical standpoint in the following section.

4. Surface wave modulation in a simplified model

Typically, wave–current interaction is studied through the framework of geometrical optics and wave action conservation, pioneered for surface waves by Longuet-Higgins and Stewart (1964) and Bretherton and Garrett (1968), and synthesized by Phillips (1966). This was applied to the surface wave IW problem by Gargettt and Hughes (1972) and Huang et al. (1972), among others. More recently, the modulation of surface waves by IW has been studied using a relaxation method (Phillips 1984; Alpers 1985; Rascle et al. 2016), with the central assumption being that the surface wave spectrum is only weakly modulated by the presence of the IW (this is *not* true in our case, as Fig. 8b explicitly illustrates). In general, bulk-scale quantities have been compared with the theory (e.g., the total energy of the surface waves). However, the measurement capabilities outlined above make it possible to check more detailed predictions of the theory, including modifications to the wind wave spectral peak and directional properties of these surface waves.

More formally, consider irrotational inviscid deep-water surface gravity waves on a current. Here, positive x corresponds to due east, while y points to the north, so that the coordinate system is right-handed. We assume the surface current has value $U(x)$ in the east direction. The intrinsic frequency is $\sigma = (g|\mathbf{k}|)^{1/2}$, with g being the acceleration due to gravity and wavenumber $\mathbf{k} = (k, l)$. Furthermore, we work in a frame moving at speed C, the phase velocity of the internal wave (Phillips 1966).

Note, we expect that the vertical shear associated with the IW-induced velocity to have a minimal effect here. The strength of the interaction of the shear flow and the surface waves is quantified by the parameter $U_{zz}/(\omega k)$ (Shrira 1993). Here, we expect the folding scale of the internal waves to be $O(10) \, \mathrm{m}$ while $\omega k \sim O(1)$ for the range of wavenumbers we will consider. Hence this ratio is small, and we do not expect the vertical shear to play an important role in this scenario.

Bretherton and Garrett (1968) showed that for slowly varying waves the wave phase obeys the following relationships. First, the total frequency ω is conserved when $\partial U/\partial t = 0$ so that

$$d\omega/dt = 0. \tag{4}$$

Here,

$$\omega = \mathbf{k} \cdot (\mathbf{U} - \mathbf{C}) + \sigma. \tag{5}$$

Next, the wavenumber satisfies the conservation of waves equation, which states

$$\frac{\partial \mathbf{k}}{\partial t} + \nabla[\sigma + \mathbf{k} \cdot (\mathbf{U} - \mathbf{C})] = \mathbf{0}. \tag{6}$$

Furthermore, because the wavenumber is the gradient of a potential function (i.e., the phase), it is irrotational, so that

$$\nabla \times \mathbf{k} = \mathbf{0}. \tag{7}$$

This implies

$$|\mathbf{k}| \sin\theta = |\mathbf{k}_0| \sin\theta_0, \tag{8}$$

where 0 represents a region far upstream of the internal wave, where there are no currents. Here, θ is the angle between the waves and the x axis (i.e., between the waves and the currents). As our system is invariant to shifts along the y axis (because the IW is assumed to have no transverse structure), Eq. (8) implies that are no modifications to the wavenumbers in the transverse direction.

From Eq. (4), the conservation of total angular frequency implies that

$$\sigma_0 - |\mathbf{k}_0|C\cos\theta_0 = |\mathbf{k}|(U - C)\cos\theta + \sigma. \tag{9}$$

An equation to specify θ may then be found by eliminating $|\mathbf{k}|$ from Eqs. (8) and (9) to give

$$\sin\theta\left(\sqrt{g|\mathbf{k}_0|} - Ck_0\cos\theta_0\right) - \mathrm{sign}(\sin\theta)\sqrt{|g|\mathbf{k}_0|\sin\theta_0\sin\theta|}$$
$$+ |\mathbf{k}_0|\sin\theta_0(C - U)\cos\theta = 0. \tag{10}$$

Note that, by letting $\sin\theta = \chi^2$, it may be readily seen that this is a quartic equation in χ that may be solved in closed form or numerically (Gargettt and Hughes 1972). Physically these equations imply waves are lengthened when traveling in the same direction as the current, and shortened when opposing, so that the directional spread of the wave field will decrease for waves on opposing flows and increase on flows going in the same direction.

In a frame following the energy ray paths, boosted into a reference frame moving at the phase velocity of the internal waves C, the wave action (Bretherton and Garrett 1968) is governed by the equation (Phillips 1966, 1984)

$$\frac{dN}{dt} = \frac{\partial N}{\partial t} + (\mathbf{c}_g + \mathbf{U} - \mathbf{C}) \cdot \nabla \mathbf{N} = \mathbf{S}, \tag{11}$$

where $\mathbf{c}_g = (\partial\sigma/\partial k, \partial\sigma/\partial l)$, $\mathbf{U}$ is the current, and $\mathbf{S}$ represents the source terms (Phillips 1985).

Hughes (1978) showed that the ray equations, and conservation of wave action, imply that in a statistically steady state we have
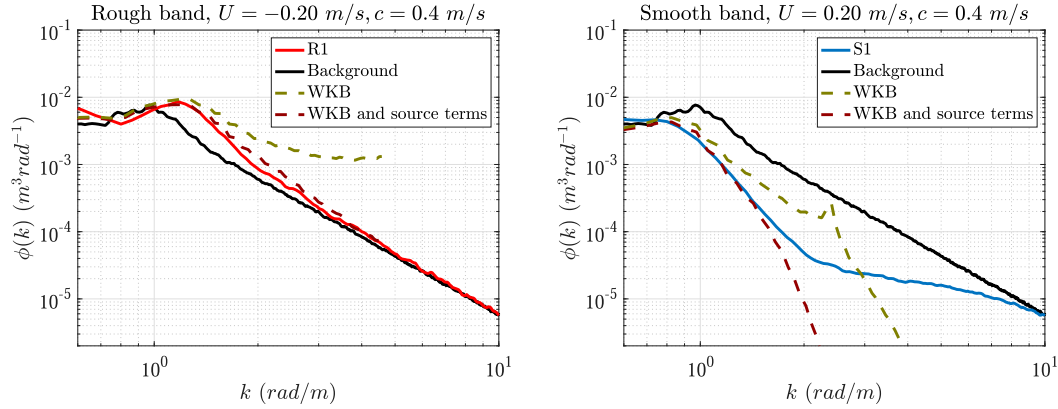
FIG. 10. Theoretical predictions of the omnidirectional spectrum of surface gravity waves. Here we examine (a) the rough-band region R1 and (b) the smooth-band region S1 defined in Fig. 6a. The phase speed of the internal wave is set to 0.4 m s^{-1} while the current speed is set to $U = -0.2$ m s^{-1} in (a) and $U = 0.2$ m s^{-1} in (b). The WKB prediction is then shown by the green dashed line, and the WKB prediction with a parameterized source function is shown by the purple dashed line. The background spectrum is plotted as a black line.

$$N\delta k\delta l_0 = N_0\delta k\delta l_0. \tag{12}$$

Now, we would like to integrate the right-hand side over k_0, so we note that the Jacobian between (k, l_0) and (k_0, l_0) may be found from the ray equations and implies that

$$(c_g - C + U)\frac{\partial k}{\partial k_0} = \frac{\partial \sigma}{\partial k_0} - C. \tag{13}$$

In terms of the energy density, we arrive at the relationship

$$F(k, l_0)\delta k\delta l_0 = F_0(k_0, l_0)\frac{\sigma}{\sigma_0}\frac{c_{g0} - C}{c_g - C + U}\delta k_0\delta l_0. \tag{14}$$

Now, we are particularly interested in comparing the omnidirectional spectrum, which here takes the form

$$\phi = \int_0^{2\pi} |\mathbf{k}|F(|\mathbf{k}|, \theta)\, d\theta, \tag{15}$$

where $|\mathbf{k}| = \sqrt{k^2 + l_0^2}$ and $\tan\theta = l_0/k$.

The theoretical prediction of the omnidirectional spectrum is displayed in Figs. 10a and 10b, which shows the WKB prediction, that is, Eq. (14) for the omnidirectional spectrum, as well as the observations of the modulated and unmodulated spectrum. Here, we take the phase velocity of the internal wave to be $C = 0.4$ m s^{-1} and the magnitude of the current to be ± 0.2 m s^{-1}.

In Fig. 10a, we see that the theory describes the observed shift in the spectral peak for waves in the rough band. However, we notice a large amplification of energy density above this peak. This is a signature of the singularity of the theory discussed above, which occurs when waves are blocked, and the theory predicts an infinite action density in this region. In particular, when $c_g - C + U$ goes to zero, we find that there is a singularity in Eq. (14). Note that we have truncated the solutions in the rough band around $k = 4.5$ rad m^{-1} for clarity of presentation. Furthermore, for waves on a smooth band, the theory does a reasonable job of describing the

spectral shift but overpredicts the spectral amplitude, as it did in the rough band.

These computations suggest that physical mechanisms might be missing from the theory, which leads to an over amplification of the dynamics of the shorter waves. For example, in the rough band, we observe wave breaking, which would dissipate the energy in these higher wavenumbers. We also find an over amplification of the energy in the smooth band that cannot be explained by breaking dissipation.

The theory described above does not account for reflected or bound waves, as it assumes all waves are traveling according to the Doppler-shifted linear dispersion relationship and that the waves travel from west to east (Smith 1983). A relatively simple theory has been developed in Craig et al. (2012), and is in agreement with a long history of studies of wave current interaction (see, e.g., Smith 1976; Peregrine 1976; Smith 1983). Craig et al. (2012) draw an analogy between surface waves on currents and a particle trapped in a potential well in quantum mechanics. From this, it may be seen that the waves may be reflected, bound, and transmitted at these scattering locations. The form of the scattering coefficients depends on the properties of the incident wavenumbers, the current magnitude, the functional form of the current field, and properties of the water column. For currents flowing in opposing direction to the wave field, reflection can occur for waves traveling at speeds below the blocking velocity, and some energy above the blocking speed might leak through these finite width current fields. Furthermore, there will be energy bound to the current fields in these locations. For waves traveling in the same direction as the currents, energy may become localized in the current region. In both scenarios, surface waves and IW may freely exchange energy. Waves in the forcing region need no longer be harmonic and can instead take on evanescent (or more complicated) forms.

Furthermore, as discussed above, waves may steepen and break when they meet an opposing current (Chawla and Kirby 2002; Ardhuin et al. 2010). The dissipation term in the wave

action balance (Phillips 1985) has recently received considerable attention, based on measurements of Phillip's wave breaking statistics, $\Lambda(\mathbf{c})$ where $\Lambda(\mathbf{c})d\mathbf{c}$ is the average breaking front lengths, per unit are of ocean surface, traveling between speeds $\mathbf{c}$ and $\mathbf{c} + d\mathbf{c}$. In particular, Sutherland and Melville (2013, 2015; see also Kleiss and Melville 2010) were able to collapse available data on a nondimensional scaling of this distribution, confirming Phillips's prediction that $\Lambda(c)$ should go like c^{-6} for larger values of c. Recently, based on contours of the slopes of exceedance (Longuet-Higgins 1957), Romero (2019) formulated a scaling of $\Lambda(c)$ that was consistent with Sutherland and Melville (2013). Note, Romero et al. (2017) found that the breaking distributions may be strongly modulated near submesoscale current features. This is an active area of research.

The discussions in the previous two paragraphs highlight the complexity of this problem. Here, we do not go into more detail on these mechanisms, but, following a similar approach to the relaxation theory often applied to SAR observations (Phillips 1984; Alpers 1985; Rascle et al. 2016), we assume that these effects can be encompassed in the source terms S, and we furthermore assume that these are related to the wave action. To this end, the simplest approach that allows for closed form solutions is to assume that $S = \mu(k_0)N(c_g + U - C)$ for some wavenumber-dependent function μ (where, for simplicity, we take the wavenumber dependence to not depend on the modulated spectra so that is independent of position). The benefit of our approach is that it leads to a simple mathematical model that is easy to interpret. A full description of this problem from first principles that physically describes wave generation by wind, wave–wave interactions, wave dissipation, and non-WKB effects (as discussed above) is outside of the scope of this paper and is an active area of research.

With the above assumptions, we find that

$$F(k, l_0)\delta k \delta l_0 = f(k_0, l_0)e^{\mu(k_0)x}\delta k \delta l_0, \qquad (16)$$

from which the modulated omnidirectional spectrum may be found. The lack of full in situ measurements does not allow us to fully constrain the model, and we fit a functional form $\mu = -3 \times 10^{-4}k_0^3/\overline{k}^2$ (where $\overline{k}$ is a constant chosen to make the exponential unitless) to the data. Here, the location x is taken to be the central location of the band under consideration.

In both the smooth and rough bands, the model describes the data over a broader range of wavenumbers than the WKB predictions alone. This is shown in Figs. 10a and 10b. In the rough bands, the parameterization seems to describe the spectral power law behavior above the wind wave peak much better than the WKB model alone, which starts to break down for larger k, as discussed above. For the smooth bands, the parameterization also leads to an improvement over the WKB model alone over a larger range of k. However, above the blocking value of k, we also find a roll-off the spectrum; the theory does not permit admissible wavenumbers above this limit. This behavior appears to be approximately consistent with the observations in this region, which also show a roll off. However, there is some wave energy in this band, possibly due to wind input.

For the wave–current interaction scenario considered here, we conclude that WKB can predict the spectral shift of the wind-wave peak for both the rough and smooth bands. However, for larger values of k the WKB model alone breaks down. It is worth reiterating that this model is coarse and does not capture individual mechanisms that may lead to additional energy modulation in a particular rough or smooth band. Specifically, it is not clear if the improvement to the model parameterizes additional physics not captured in the action evolution equation (e.g., bound energy or wave reflection) or if it parameterizes effects due to input terms in the wave action balance (e.g., wave breaking or wind input). This is a topic of considerable interest that will be examined in a future study, as to fully address this one would need phase resolved measurements of the wave field, wave breaking statistics, and high-resolution measurements of the IW-induced surface currents.

5. Discussion and summary

In this paper, the interaction between surface and internal waves is investigated using a combination of airborne remote sensing observations, in situ surface and subsurface measurements, and theoretical (i.e., geometrical optics and wave action conservation) predictions. Many common assumptions about the behavior of the wave slope (e.g., assuming its deviations due to these interactions are small) are explicitly examined.

Properties of the surface slope as it varies across the internal wave packet is investigated using the lidar-derived surface topography. We find significant modulation of the mean-square slope over very short distances (up to a factor-of-2 increase or decrease in mean square slope magnitude over less than a few hundred meters). More broadly, this highlights the importance of wave–current interaction processes in modulating surface roughness. As the spatial resolution of orbital remote sensing instruments is improving, and the role of submesoscale processes in upper-ocean dynamics has been identified as a critical science area for future research, we can no longer ignore these effects. The slope ratio γ, a measure of the directionality of the total surface slope, is also rapidly modulated under the influence of the internal wave packet. We find that the directional properties of the surface wave field become almost isotropic in smooth bands and exhibit increased anisotropy in the rough bands.

The spatial evolution of the directional and omnidirectional spectra was examined, showing rapid modulation of the directional and spectral properties of the surface waves by the propagating internal wave packet, concentrated in the 0.6–10-m range of surface wave wavelength, leading to the generation of a series of rough and smooth bands, the classical characteristic surface signature of internal waves. This modulation, caused by wave–current interaction processes, is directly observed, and investigated from a theoretical standpoint. We find that basic geometrical optics and wave action theory, pioneered by Phillips (1966), Longuet-Higgins and Stewart (1962, 1964), and Bretherton and Garrett (1968), works well for describing the wind-wave spectral shift due to the currents, found in the omnidirectional wave spectrum. However, the theory breaks down for higher wavenumbers where the singularity

predicted due to wave blocking becomes severe. It is hypothesized that this is partially due to the inability of this ray theory argument to quantify wave reflection and trapping due to the currents, and the fact that other physical processes like wave breaking are not included in this model. Generically, we have parameterized these processes, and found agreement with the observations over a larger range of wavenumbers. However, a more detailed examination, and a more general axiomatic model, will be pursued in a future study.

There are also many features of the internal waves that motivate discussion. Figure 3 and 5a show the presence of transverse thermal structure, even as the internal wave fronts remain quasi one dimensional. These structures may be due to transverse instabilities (steep internal waves suffer from a transverse instability in much the same way as steep surface waves (see Pullin and Grimshaw 1985) that may lead to internal wave overturning, or some other mechanism that causes vertical flux of cold water to the surface. This warrants future attention.

The physical scenario considered here, that is, the modulation of surface waves due to a compact internal wave, should also yield insight into surface gravity wave–submesoscale current (McWilliams 2016) interaction processes that could be considered as analogous to a superposition of events like the one examined here.

Data availability statement. All presented data are available at the UCSD Library Digital Collection (https://library.ucsd.edu/dc).

REFERENCES

Alpers, W., 1985: Theory of radar imaging of internal waves. *Nature*, **314**, 245–247, https://doi.org/10.1038/314245a0.

Ardhuin, F., and Coauthors, 2010: Semiempirical dissipation source functions for ocean waves. Part I: Definition, calibration, and validation. *J. Phys. Oceanogr.*, **40**, 1917–1941, https://doi.org/10.1175/2010JPO4324.1.

Bréon, F., and N. Henriot, 2006: Spaceborne observations of ocean glint reflectance and modeling of wave slope distributions. *J. Geophys. Res.*, **111**, C06005, https://doi.org/10.1029/2005JC003343.

Bretherton, F. P., and C. J. R. Garrett, 1968: Wavetrains in inhomogeneous moving media. *Proc. Roy. Soc. London*, **302A**, 529–554, https://doi.org/10.1098/rspa.1968.0034.

Chawla, A., and J. T. Kirby, 2002: Monochromatic and random wave breaking at blocking points. *J. Geophys. Res.* **107**, 3067, https://doi.org/10.1029/2001JC001042.

Cox, C., and W. Munk, 1954: Measurement of the roughness of the sea surface from photographs of the sun's glitter. *J. Opt. Soc. Amer.*, **44**, 838–850, https://doi.org/10.1364/JOSA.44.000838.

Craig, W., P. Guyenne, and C. Sulem, 2012: The surface signature of internal waves. *J. Fluid Mech.*, **710**, 277–303, https://doi.org/10.1017/jfm.2012.364.

Deike, L., N. Pizzo, and W. K. Melville, 2017: Lagrangian transport by breaking surface waves. *J. Fluid Mech.*, **829**, 364–391, https://doi.org/10.1017/jfm.2017.548.

Gargettt, A., and B. Hughes, 1972: On the interaction of surface and internal waves. *J. Fluid Mech.*, **52**, 179–191, https://doi.org/10.1017/S0022112072003027.

Hao, X., and L. Shen, 2020: Direct simulation of surface roughness signature of internal wave with deterministic energy-conservative model. *J. Fluid Mech.*, **891**, R3, https://doi.org/10.1017/jfm.2020.200.

Helfrich, K. R., and W. K. Melville, 2006: Long nonlinear internal waves. *Annu. Rev. Fluid Mech.*, **38**, 395–425, https://doi.org/10.1146/annurev.fluid.38.050304.092129.

Huang, N. E., D. T. Chen, C.-C. Tung, and J. R. Smith, 1972: Interactions between steady won-uniform currents and gravity waves with applications for current measurements. *J. Phys. Oceanogr.*, **2**, 420–431, https://doi.org/10.1175/1520-0485(1972)002<0420:IBSWUC>2.0.CO;2.

Hughes, B. A., 1978: The effect of internal waves on surface wind waves 2. Theoretical analysis. *J. Geophys. Res.*, **83**, 455–465, https://doi.org/10.1029/JC083iC01p00455.

Jiang, S. W., G. Kovačič, D. Zhou, and D. Cai, 2019: Modulation-resonance mechanism for surface waves in a two-layer fluid system. *J. Fluid Mech.*, **875**, 807–841, https://doi.org/10.1017/jfm.2019.501.

Kleiss, J. M., and W. K. Melville, 2010: Observations of wave breaking kinematics in fetch-limited seas. *J. Phys. Oceanogr.*, **40**, 2575–2604, https://doi.org/10.1175/2010JPO4383.1.

——, and ——, 2011: The analysis of sea surface imagery for whitecap kinematics. *J. Atmos. Oceanic Technol.*, **28**, 219–243, https://doi.org/10.1175/2010JTECHO744.1.

Kumar, N., and Coauthors, 2021: The Inner-Shelf Dynamics Experiment. *Bull. Amer. Meteor. Soc.*, **102**, E1033–E1063, https://doi.org/10.1175/BAMS-D-19-0281.1.

Lenain, L., and W. K. Melville, 2017: Measurements of the directional spectrum across the equilibrium saturation ranges of wind-generated surface waves. *J. Phys. Oceanogr.*, **47**, 2123–2138, https://doi.org/10.1175/JPO-D-17-0017.1.

——, and N. Pizzo, 2020: The contribution of high frequency wind-generated surface waves to the Stokes drift. *J. Phys. Oceanogr.*, **50**, 3455–3465, https://doi.org/10.1175/JPO-D-20-0116.1.

——, ——, and W. K. Melville, 2019a: Laboratory studies of Lagrangian transport by breaking surface waves. *J. Fluid Mech.*, **876**, R1, https://doi.org/10.1017/jfm.2019.544.

——, N. M. Statom, and W. K. Melville, 2019b: Airborne measurements of surface wind and slope statistics over the ocean. *J. Phys. Oceanogr.*, **49**, 2799–2814, https://doi.org/10.1175/JPO-D-19-0098.1.

Longuet-Higgins, M. S., 1957: The statistical analysis of a random, moving surface. *Philos. Trans. Roy. Soc. London*, **249A**, 321–387, https://doi.org/10.1098/rsta.1957.0002.

——, and R. Stewart, 1962: Radiation stress and mass transport in gravity waves, with application to 'surf beats.' *J. Fluid Mech.*, **13**, 481–504, https://doi.org/10.1017/S0022112062000877.

——, and ——, 1964: Radiation stresses in water waves; A physical discussion, with applications. *Deep-Sea Res. Oceanogr. Abstr.*, **11**, 529–562, https://doi.org/10.1016/0011-7471(64)90001-4.

McKee, W., 1975: A two turning-point problem in fluid mechanics. *Math. Proc. Cambridge. Philos. Soc.*, **77**, 581–590, https://doi.org/10.1017/S0305004100051409.

McSweeney, J. M., and Coauthors, 2020: Observations of shoaling nonlinear internal bores across the central California inner shelf. *J. Phys. Oceanogr.*, **50**, 111–132, https://doi.org/10.1175/JPO-D-19-0125.1.

McWilliams, J. C., 2016: Submesoscale currents in the ocean. *Proc. Roy. Soc. London*, **472A**, 20160117, https://doi.org/10.1098/rspa.2016.0117.

Melville, W. K., L. Lenain, D. R. Cayan, M. Kahru, J. P. Kleissl, P. Linden, and N. M. Statom, 2016: The modular aerial sensing system. *J. Atmos. Oceanic Technol.*, **33**, 1169–1184, https://doi.org/10.1175/JTECH-D-15-0067.1.

Munk, W., 2009: An inconvenient sea truth: Spread, steepness, and skewness of surface slopes. *Annu. Rev. Mar. Sci.*, **1**, 377–415, https://doi.org/10.1146/annurev.marine.010908.163940.

Osborne, A., and T. Burch, 1980: Internal solitons in the Andaman Sea. *Science*, **208**, 451–460, https://doi.org/10.1126/science.208.4443.451.

Peregrine, D., 1976: Interaction of water waves and currents. *Adv. Appl. Mech.*, **16**, 9–117, https://doi.org/10.1016/S0065-2156(08)70087-5.

Phillips, O., 1966: *The Dynamics of the Upper Ocean*. Cambridge University Press, 269 pp.

——, 1984: On the response of short ocean wave components at a fixed wavenumber to ocean current variations. *J. Phys. Oceanogr.*, **14**, 1425–1433, https://doi.org/10.1175/1520-0485(1984)014<1425:OTROSO>2.0.CO;2.

——, 1985: Spectral and statistical properties of the equilibrium range in wind-generated gravity waves. *J. Fluid Mech.*, **156**, 505–531, https://doi.org/10.1017/S0022112085002221.

Pizzo, N., W. K. Melville, and L. Deike, 2019: Lagrangian transport by nonbreaking and breaking deep-water waves at the ocean surface. *J. Phys. Oceanogr.*, **49**, 983–992, https://doi.org/10.1175/JPO-D-18-0227.1.

Plant, W. J., W. C. Keller, K. Hayes, G. Chatham, and N. Lederer, 2010: Normalized radar cross section of the sea for backscatter: 2. Modulation by internal waves. *J. Geophys. Res.*, **115**, C09033, https://doi.org/10.1029/2009JC006079.

Pullin, D., and R. Grimshaw, 1985: Stability of finite-amplitude interfacial waves. Part II: Numerical results. *J. Fluid Mech.*, **160**, 317–336, https://doi.org/10.1017/S0022112085003500.

Rascle, N., F. Nouguier, B. Chapron, A. Mouche, and A. Ponte, 2016: Surface roughness changes by finescale current gradients: Properties at multiple azimuth view angles. *J. Phys. Oceanogr.*, **46**, 3681–3694, https://doi.org/10.1175/JPO-D-15-0141.1.

Romero, L., 2019: Distribution of surface wave breaking fronts. *Geophys. Res. Lett.*, **46**, 10 463–10 474, https://doi.org/10.1029/2019GL083408.

——, L. Lenain, and W. K. Melville, 2017: Observations of surface wave–current interaction. *J. Phys. Oceanogr.*, **47**, 615–632, https://doi.org/10.1175/JPO-D-16-0108.1.

Shrira, V. I., 1993: Surface waves on shear currents: Solution of the boundary-value problem. *J. Fluid Mech.*, **252**, 565–584, https://doi.org/10.1017/S002211209300388X.

Smith, J., 1983: On surface gravity waves crossing weak current jets. *J. Fluid Mech.*, **134**, 277–299, https://doi.org/10.1017/S0022112083003365.

Smith, R., 1976: Giant waves. *J. Fluid Mech.*, **77**, 417–431, https://doi.org/10.1017/S002211207600219X.

Sutherland, P., and W. K. Melville, 2013: Field measurements and scaling of ocean surface wave-breaking statistics. *Geophys. Res. Lett.*, **40**, 3074–3079, https://doi.org/10.1002/grl.50584.

——, and ——, 2015: Field measurements of surface and near-surface turbulence in the presence of breaking waves. *J. Phys. Oceanogr.*, **45**, 943–965, https://doi.org/10.1175/JPO-D-14-0133.1.

Thomas, M., S. Misra, C. Kambhamettu, and J. T. Kirby, 2005: A robust motion estimation algorithm for PIV. *Meas. Sci. Technol.*, **16**, 865–877, https://doi.org/10.1088/0957-0233/16/3/031.

Thompson, D., and R. Gasparovic, 1986: Intensity modulation in SAR images of internal waves. *Nature*, **320**, 345–348, https://doi.org/10.1038/320345a0.